Feature extractions by Proper Orthogonal Decomposition and Bidirectional Gated Recurrent Units for identifying ship collisions to offshore wind turbine

Lihua Liu [a], Huijuan Liu [a], Dianzi Liu [a,c], Fushun Liu [a,b,*]

[a] College of Engineering, Ocean University of China, Qingdao 266100, China

[b] Shandong Province Key Laboratory of Ocean Engineering, Ocean University of China, Qingdao 266100, China

[c] School of Engineering, University of East Anglia, Norwich, NR14 7TH, United Kingdom

Abstract

Timely detection and termination of ship collisions to offshore wind turbine are essential to ensure the structural integrity and sustainability of marine applications. The collision identification through sensors, such as accelerometers mounted on structures, is simpler and more reliable than non-contact collision methods. However, this approach is susceptible to the environmental complexities, leading to potential misjudgements. To mitigate this issue, a collision identification architecture, called ColliNet, utilising a Bidirectional Gated Recurrent Unit (BiGRU) neural network with the integration of Proper Orthogonal Decomposition (POD) and time-frequency fusion (TFF) techniques, is proposed for the impact analysis of ship-offshore wind turbine. This architecture is realized by two phases of feature processing in prediction and classification, respectively. Firstly, the critical features of time evolution coefficients are extracted from the acceleration response predicted by the POD feature extraction block. Afterwards, the fused time-frequency domains of the time evolution coefficient features are fed into the BiGRU feature classification block to further extract the features related to the operation condition. ColliNet, constrained by user-defined loss functions with physical information imposed, reliably explains the complex response patterns of the wind turbines under long-term operating conditions. It also reduces the spatial complexity of the signal due to the removal of structure-related modal information. The effectiveness of the developed architecture is validated by numerical simulations using OpenFAST with the implementation of ship-turbine collision module. The collisions under different operating conditions are successfully identified with an accuracy improvement of over 6.7% on the testing dataset compared to the BiGRU network. Moreover, lab-scale collision tests are conducted on an NREL 5-MW monopile wind turbine (1:70 scale) to further demonstrate the validity of the ColliNet architecture. The proposed architecture is able to provide reliable support for maintenance measures and helps to realize the autonomous monitoring in replacement with visual inspection using high-definition camera systems, thereby mitigating the operation and maintenance cost of wind turbines while improving their reliability and sustainability.

Keywords

Offshore wind turbines; Ship collision identification; ColliNet architecture; Time evolution coefficients; BiGRU network; Time-frequency domain fusion.

1. Introduction

The reliable in-service operation of offshore engineering structures is critical for the exploitation of marine resources. Damage of these structures can stem from various sources including falling objects, collisions, fatigue, design modifications, welding failures, concrete construction defects, etc. In extreme cases, external loads may cause collapse of an entire structure, leading to severe economic losses and

* Corresponding author.

Email address: percyliu@ouc.edu.cn (Fushun Liu)

environmental pollution (Song et al., 2021). Tebbett (1987) investigated 100 offshore platforms requiring repair, finding that over 25% of structural damage cases were related to collisions. In addition to environmental loads, offshore structures are also susceptible to collisions caused by operational errors of passing ships during navigation or routine maintenance. This is particularly relevant to offshore wind farms, where transport and service ships frequently access wind turbines for inspection, maintenance and repair. These operations involve complex berthing and manoeuvring in a high-energy marine environment, increasing the risk of accidental collisions. Dai et al. (2013) analysed collision risk data for offshore oil and gas installations and found that over 96% of collisions were generated by service ships. Although most of these collisions were low-energy events causing minor damage, there were five cases involved in significant structural damage. Given the rapid expansion of offshore wind energy and the increasing reliance on service ships for maintaining wind turbines, understanding and mitigating collision risks during routine operations is critical to ensuring the structural integrity and long-term reliability of offshore assets.

The collision between a ship and an offshore structure involves complex external and internal dynamics, which are typically decoupled analysis. External collision dynamics focuses on the dynamic response of both the ship and collided structure, and is primarily solved by dynamic motion equations. Minorsky et al. (1958) first tried to separate external and internal collision mechanics for the extent of penetrations in ship collisions, and proposed the concept of additional mass. On this basis, Seizo et al. (1971) provided an exact expression for the hydrodynamic force acting on a ship during a collision and conducted model tests to validate their theoretical findings, further advancing the study of ship collisions. Petersen (1981) utilised numerical simulations to examine the collision process between a ship and a floating platform, correlating the additional mass coefficients of the ships with hydrodynamic coefficients of finite frequency. Based on the general theory of rigid body collision mechanics, Zhang and Pedersen (1999) analysed the energy dissipation during ship collision and derived the relationship between the initial ship kinetic energy and the energy stored in the system after the collision. The study of external collision dynamics typically involves analytical and numerical methods, though the simplified model of nonlinear springs limits the accuracy in predicting structural deformation. Therefore, both external and internal dynamics should be considered to achieve more accurate results. The internal dynamics mainly studies the damage and deformation of the structure in the collision area as well as the collision force and energy loss. To solve this problem, there are four main methods including empirical formula, simplified analytical, experimental, and finite element simulation. The empirical formula method is the earliest and most comprehensive approach. The simplified analytical method uses a combination of theory and experience to analyse the collision process based on some basic mechanical theories and reasonable model assumptions. This method has been widely used in the study of energy absorption distribution and failure criterion during collision, as it has the ability to obtain the results quickly and reliably (Chang et al., 1980; Kinkead, 1980; Reckling, 1983). Since both the empirical and simplified methods require test data, numerical analysis has become the dominant research method, with LS-DYNA software widely used for simulating collisions (De Oliveria, 1981; Zhu et al., 1994; Zhu and Faulkner, 1991).

With the increasing number of marine engineering equipment and its ageing structures, the demand for structural maintenance is growing rapidly. Improving the identification method of collision between ships and offshore engineering structures and implementing protective measures at the onset of collision can effectively prevent further structural damage, which is of great significance to the safe operation of marine engineering equipment. Current ship collision identification and prevention technologies fall into

two categories: non-contact and contact methods. Non-contact techniques mainly include Light Detection and Ranging (LiDAR), high-definition (HD) cameras, and automatic identification systems (AIS). LiDAR provides high measurement accuracy, broad scanning range, and strong environmental adaptability. However, it is expensive and has high error margins in long-distance measurements. Thus, it was vulnerable to tampering or adverse weather conditions (Ma et al., 2023). HD cameras offer detailed real-time images, but their effectiveness is limited by poor data transmission stability and visibility issues due to weather conditions (Wei et al., 2018). AIS improves maritime traffic management by automatically collecting and transmitting data such as the position, heading, and velocity of ships, but its functionality relies on uninterrupted power and communication infrastructure. In contrast, contact technology provides a direct and specific monitoring method, which relies on sensors installed on structures to monitor ship collision by detecting changes in sensor values (Rong et al., 2022). Among these techniques, acceleration sensors have been commonly used in offshore structure monitoring owing to their ease of installation, low cost, and high accuracy, though they are also susceptible to environmental noise and electromagnetic interference.

In the fields of transportation, ocean engineering, and bridge structures, key terms related with collision studies are shown in Fig. 1 (a). It is noted that studies with keywords such as 'collision avoidance', 'machine learning', and 'neural network' are increasingly paid more attention by scholars, as shown in Fig. 1 (b). As a powerful tool for artificial intelligence, machine learning methods have been applied with great success in many different fields outside of computer science. Before the formal training of the model, data pre-processing is essential, including steps such as data cleaning, feature selection and dimensionality reduction, data normalisation, and data augmentation (Maharana et al., 2022). These processes aim to reduce the complexity of machine learning and improve the accuracy of the model. For complex datasets, feature selection and dimensionality reduction are particularly important as they reduce redundant information by selecting highly correlated features or applying dimensionality reduction techniques, thereby enhancing the training efficiency of the model. Common dimensionality reduction methods include Principal Component Analysis (PCA) and Linear Discriminant Analysis (LDA) (Pule et al., 2022). Among these, Proper Orthogonal Decomposition (POD), as a generalisation of PCA in a broader function space, has been successfully applied to reduce the dimensionality of high-dimensional datasets, particularly in the analysis of spatial-temporal data in fluid flow fields. By extracting the most dominant patterns from these datasets, POD helps identify key features while simultaneously reducing computational costs. Since abnormal data diagnosis is often framed as classification problems, most abnormal data studies employ supervised learning methods, such as Convolutional Neural Networks (CNN) for dual-channel time-frequency visualisation (Tang et al., 2019), Backpropagation (BP) neural networks (Zhang et al., 2010), random forests, naive Bayes (Casali et al., 2021), logistic regression (Zadrozny et al., 2003), Long-Short Term Memory (LSTM) (Guo et al., 2020), LSTM-AE multivariate multiscale self-encoder (Kammoun et al., 2023), Gated Recurrent Unit (GRU) neural networks (Husari and Seshadrinath, 2022), Wildnet classification networks, and time domain convolutional networks (TCN) (Zhao et al., 2023) . In particular, as a variant of GRU, Bidirectional GRU (BiGRU) excels at capturing past and future time dependencies in continuous data, which is potentially useful for predicting and classifying events over time (Zhu et al., 2019). Unsupervised methods like density-based clustering (Brighenti and Sanz-Bobi, 2011), K-means (Yiakopoulos et al., 2011), deep convolutional generative adversarial networks (DCGAN) (Radford et al., 2015), kernel density estimation (Xue et al., 2020), and deep confidence networks (DBN) (Su et al., 2021) are also employed. Most of the above methods has been used for fault identification of structures,

and collision identification can be regarded as a special fault identification problem, which can also be studied by machine learning methods. In particular, deep learning model can identify complex collision patterns by learning from a large amount of historical data without relying on predefined theoretical models, and can better adapt to a variety of complex environmental conditions. At the same time, it can capture subtle patterns and correlations that are difficult to discover manually, thus improving the accuracy of the collision identification.

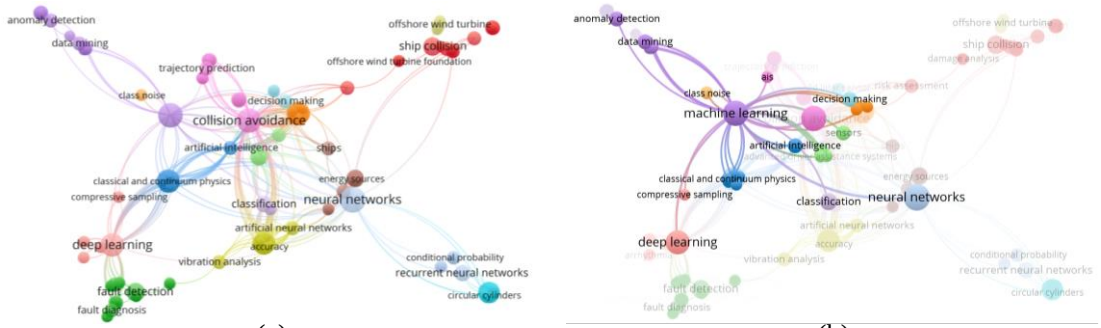

Fig. 1. Network visualisation of keywords in collision studies: (a) Overall view; (b) Local zoom in relation to keywords for 'machine learning'.

Research on ship collision has mainly focused on early warnings of ship navigation risk before the collision and post-collision damage analysis of the structure, with limited studies on real-time collision monitoring and identification. The existing collision identifications are primarily traditional physical methods, which exhibit limited resilience to signal interference difficulty in adapting to varying environmental conditions, and slower response times. Deep learning methods, while effective, require large amounts of data. The intricate operating conditions of wind turbines, coupled with the infrequency of ship collision, make it challenging to collect adequate collision data. To address these challenges, a ColliNet architecture that synergizes POD and BiGRU for real-time collision identification using the limited data is proposed in this study. The main innovations and advantages of the proposed method are demonstrated from two aspects:

(1) Noise Robustness: By isolating the intrinsic dynamics of the collision from the ambient noise through POD's mode truncation, the architecture outperforms the conventional accelerometers and stand-alone BiGRU models in noisy marine environments. This advantage agrees with the findings of POD in denoising high-dimensional data (Brindise and Vlachos, 2017).

(2) Spatio-temporal interpretability: Though CNNs excel at spatial feature extractions, they often ignore temporal dependencies. BiGRU explicitly models bi-directional time-series relationships to capture pre- and post-collision dynamics, thereby improving the classification accuracy. In our testing stage, the accuracy of the POD-BiGRU framework is 7%-8% higher than that of traditional LSTM and CNN models.

The remainder of this paper is organised as follows: Section 2 discusses the underlying theory. Section 3 outlines the proposed collision identification architecture. Sections 4 and 5 validate the architecture using numerical simulation data from the implemented OpenFAST and lab-scale test data, respectively. The final section concludes the paper.

2. Preliminaries

To address the challenges of ship collision identification posed by complex environments and limited data, this section analyses the core methodologies from a theoretical perspective. Given the high-dimensional characteristics of acceleration signals during collision events, the POD method is introduced

to eliminate redundant information and retain key dynamical patterns. Additionally, the GRU model is employed to effectively capture the temporal evolution of acceleration signals, realizing its efficient memory and update mechanisms. The mathematical principles underlying the POD method and the structural characteristics and suitability of the GRU model are described in detail below.

2.1 POD method

POD method is a data decomposition technique grounded in statistical analysis, primarily employed to extract low-dimensional eigenmodes from high-dimensional datasets (Li et al., 2021). By computing the covariance matrix of the data and decomposing its eigenvalues, POD generates a set of orthogonal basis vectors that optimally represent the raw data. These primary POD modes facilitate dimensionality reduction while preserving the key features of the data. Compared to the traditional PCA, POD is more suitable for processing continuous time series data, such as information observed from flow fields and vibration.

Assume that the bitwise space variable of the structure in a two-dimensional system is denoted as $\boldsymbol{y}\left(x,t\right)$, where x denotes the position and t represents the time series. For the j^{th} discrete time series, it can be represented as $\boldsymbol{y}\left(x,t_j\right)$, $j\in\left[1,M\right]$, where M denotes the number of measurement points. The data for all time steps can be written in a form of the snapshot ensemble matrix. Suppose this data can be projected onto a space spanned by a set of complete orthogonal canonical basis functions, $\boldsymbol{\Phi}=\left[\phi_1\left(x\right),\cdots,\phi_M\left(x\right)\right]$:

$$\boldsymbol{y}\left(x,t_j\right)=\sum_{i=1}^{N_t}a_i\left(t_j\right)\phi_i\left(x\right), \tag{1}$$

where N_t represents the length of the time series and $a_i\left(t_j\right)$ denotes the modal coefficient of the i^{th} orthogonal canonical basis at the j^{th} moment.

This set of orthogonal basis functions $\boldsymbol{\Phi}$ is determined by maximising the following quantity:

$$\boldsymbol{\Phi}=\arg\max\left[\frac{1}{M}\sum_{j=1}^{M}|\left(\boldsymbol{y}(x,t_j)\cdot\boldsymbol{\Phi}\right)|^2\right],\left(\boldsymbol{\Phi},\boldsymbol{\Phi}\right)=1, \tag{2}$$

where the dot $(\cdot)$ represents the inner product.

The Eq. (2) can be solved by defining an appropriate kernel function and an operator between the kernel function and the desired basis.

2.2 GRU model

Recurrent Neural Network (RNN) is designed to model data sequences like time series (Cho et al., 2014). The GRU is a type of RNN that, like LSTM, is proposed to solve the long-term memory and gradient problems in backpropagation. In LSTM, three gate functions including input gate, forgetting gate, and output gate, are introduced to control the input, memory, and output values, respectively. In contrast, there are only two gates in the GRU model: the update gate and the reset gate. The specific structure is illustrated in Fig. 2.

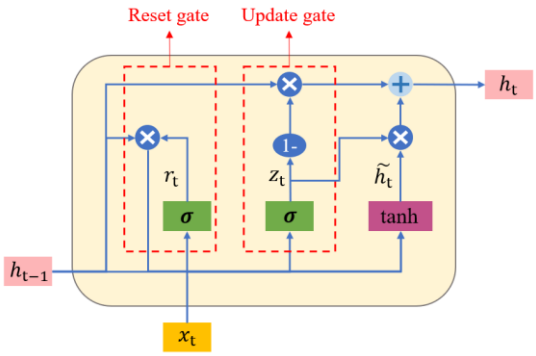

Fig. 2. The structure of the GRU model.

It is noted that the output h_t and input h_{t-1} represent the states at times t and $t-1$, respectively. x_t denotes an auxiliary input that depends on the previous time of $t-1$. r_t signifies the reset gate, z_t specifies the update gate. Rectangles indicate neural network layers and circle lines depict entry-wise operations. Bifurcations stand for copy operations and the joined lines mean the action of concatenation. The GRU state h_t is a linear interpolation of the previous state h_{t-1} and a candidate state $\tilde{h}_t$. The candidate state $\tilde{h}_t$ is a function of the unit input x_t and the previous state h_{t-1}. The GRU process is formulated as follows:

$$\begin{cases} z_t = \sigma\left(W_z x_t + U_z h_{t-1} + b_z\right) \\ r_t = \sigma\left(W_r x_t + U_r h_{t-1} + b_r\right) \\ \tilde{h}_t = \tanh\left(W x_t + U(r_t \circ h_{t-1}) + b\right) \\ h_t = (1 - z_t) \circ h_{t-1} + z_t \circ \tilde{h}_t, \end{cases} \tag{3}$$

where $(\circ)$ means the entry-wise (Hadamard) product, σ denotes the sigmoid function, and W, U, and b are trainable parameters which implicitly depend on t. GRU mixes neuron states and hidden states simultaneously, which can effectively alleviate the problem of 'gradient disappearance' in RNN networks and reduce the number of parameters represented in LSTM network units, therefore shortening the model training time.

3. The proposed collision identification architecture

To address the poor anti-interference ability of traditional physical methods, the need for large amounts of data, and weak interpretability of machine learning, an architecture (ColliNet) combining the POD-based feature extraction with BiGRU-based feature classification is proposed in this paper to identify ship-wind turbine collisions using limited samples. As illustrated in Fig. 3, the feature processing carried out in two phases. In the first phase, the Artificial Neural Network (ANN) is constrained by the physical information of the signals obtained via POD to predict the time evolution coefficients. In the second phase, these coefficients are transformed into the frequency domain, and by combining both time and frequency domain evolution coefficients, time-frequency domain fusion (TFF) features are generated. These TFF features are then fed into the BiGRU network for data classification.

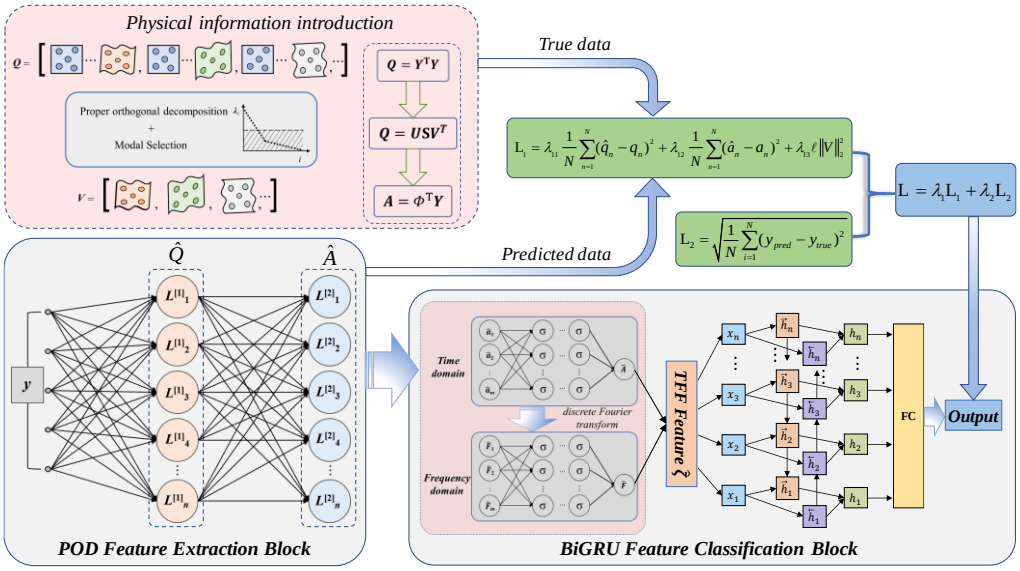

Fig. 3. The proposed ColliNet architecture for collision identification.

Multiple sensors are typically arranged along the spreading direction of wind turbines to collect data including acceleration, wind speed and tower rotor speed for effectively capturing the structural vibration characteristics. Moreover, the use of accelerometers in this study has the advantages of ease installation, low cost, and high accuracy. Given the non-stationary nature of the raw signals, it is necessary to de-average and normalise the data for the following dynamic analysis. The max-min normalisation process ensures greater stability and optimisation speed, scaling the data linearly in the range of 0 to 1. The main approach to mining characteristic information from the acceleration response of wind turbines is to discover the variation patterns from the time series. Nevertheless, collisions between wind turbines and ships, especially traffic ships, are infrequent and usually take only a few seconds. To simplify data processing, the raw signal is segmented into the intervals of T seconds.

The marine environment, characterised by waves and wind, generates considerable noise. This noise can obscure the natural vibration frequencies of the turbine structure, thereby affecting acceleration measurements. To obtain precise vibration data and improve the system's resilience to noise, filtering is essential to eliminate irrelevant frequency components. The Fourier transform enables the conversion of time-domain signals to the frequency domain, facilitating the differentiation between noise and structural vibration frequencies (Hinich et al., 2009). Since marine noise often has distinct frequency characteristics, setting a frequency threshold allows effective noise removal. The discrete Fourier transform (DFT) efficiently handles this process, ensuring both speed and accuracy. Specifically, the time-domain signal undergoing a DFT produces the frequency spectrum and an appropriate frequency range is then selected for filtering. Following this, inverse Fourier transform is applied to convert the filtered signal to the time domain, yielding a more accurate vibration response.

For a structure with m measurement points distributed along the axial direction, the spatial field of the filtered response $\boldsymbol{y}_{N_t\times m}$ can be expressed as

$$\boldsymbol{y}_{N_t\times m}=\left\{y\left(t_1,x\right),y\left(t_2,x\right),\cdots,y\left(t_{N_t},x\right)\right\}^{\mathrm{T}}=\begin{bmatrix} y\left(t_1,x_1\right) & y\left(t_1,x_2\right) & \cdots & y\left(t_1,x_m\right)\\ y\left(t_2,x_1\right) & y\left(t_2,x_2\right) & \cdots & y\left(t_2,x_m\right)\\ \vdots & \vdots & \ddots & \vdots\\ y\left(t_{N_t},x_1\right) & y\left(t_{N_t},x_2\right) & \cdots & y\left(t_{N_t},x_m\right)\end{bmatrix}, \tag{4}$$

where N_t is the length of the time series, t_{N_t} denotes the N^{th} point of the time series, x_m represents the m^{th} measurement point, and $y\left(t_{N_t}, x_m\right)$ indicates the acceleration response at the spatial field time of t_{N_t} and the location of x_m.

For the time evolution coefficients of the first m^{th} POD modes, a three-layer ANN architecture is designed as shown in Fig. 4. Here, the element of the predicted time evolution coefficient $\hat{\boldsymbol{A}}$ at moment t is denoted as $\hat{a}(t)$, and the ANN can be used to capture the changing patterns in the time series and the output layer is as follows:

$$\begin{aligned}\hat{\boldsymbol{A}} &= \sum_{i=1}^{N_t} \hat{a}_i(t) = f_L\left(\left\{y(t_1, x), y(t_2, x), \cdots, y\left(t_{N_t}, x\right)\right\}^{\mathrm{T}}; \boldsymbol{\theta}_L\right) \\ &= f_L\left(\boldsymbol{\mathcal{K}}(\boldsymbol{y}, \boldsymbol{Q}, \boldsymbol{A}); \boldsymbol{\theta}_L\right),\end{aligned} \tag{5}$$

where L denotes the L^{th} layer of ANN, f_L stands for the mapping function, $\boldsymbol{\theta}_L$ represents the network training parameter, $\boldsymbol{\mathcal{K}}$ indicates the nonlinear operator mapping the input signal to the output, $\boldsymbol{y}$ refers to the filtered acceleration time series, $\boldsymbol{Q}$ indicates the covariance matrix of $\boldsymbol{y}$ used to constrain the first layer of the ANN, and $\boldsymbol{A}$ represents the true value of time evolution coefficient used to constrain the second layer of the ANN.

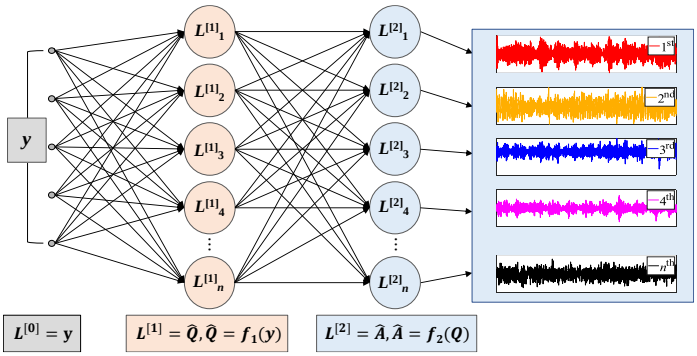

Fig. 4. ANN-based POD feature extraction block.

Furthermore, to satisfy the orthogonality of the parameters as in Eq. (2), regularisation constraint is imposed on the ANN. Therefore, the loss function of the ANN-based POD feature extraction block is expressed as

$$\mathrm{L}_1 = \lambda_{11}\frac{1}{N}\sum_{n=1}^{N}(\hat{q}_n - q_n)^2 + \lambda_{12}\frac{1}{N}\sum_{n=1}^{N}(\hat{a}_n - a_n)^2 + \lambda_{13}\ell\|V\|_2^2, \tag{6}$$

where N denotes the total number of samples, $\hat{q}_n$ and q_n refer the n^{th} predicted and true values of $\boldsymbol{Q}$, respectively, $\hat{a}_n$ and a_n signify the n^{th} predicted and true values of $\boldsymbol{A}$, respectively. $\frac{1}{N}\sum_{n=1}^{N}(\hat{q}_n - q_n)^2$ represents Mean Squared Error (MSE) loss of the first layer of the ANN-based POD feature extraction block, $\frac{1}{N}\sum_{n=1}^{N}(\hat{a}_n - a_n)^2$ indicates the MSE loss of its second layer, V stands for the network parameter trained in the output layer, and $\ell\|V\|_2^2$ means the regularisation loss to mitigate overfitting, λ_{11}, λ_{12}, and λ_{13} represent the weight of each item.

The modal information related to the structure is removed after obtaining the predicted first *m*-order time evolution coefficients $\hat{\boldsymbol{A}}$, which reduces the spatial-temporal complexity of the signal. In addition, a supervised method is used to train this feature extraction block, in which Eq. (1) is applied to extract the time evolution coefficients $\boldsymbol{A}$ as the true data:

$$\boldsymbol{A}=\boldsymbol{\Phi}^{\mathrm{T}}\boldsymbol{y}=\begin{Bmatrix}\varphi_1\\ \varphi_2\\ \vdots\\ \varphi_m\end{Bmatrix}\begin{bmatrix} y\left(t_1,x_1\right) & y\left(t_1,x_2\right) & \cdots & y\left(t_1,x_m\right)\\ y\left(t_2,x_1\right) & y\left(t_2,x_2\right) & \cdots & y\left(t_2,x_m\right)\\ \vdots & \vdots & \ddots & \vdots\\ y\left(t_{N_t},x_1\right) & y\left(t_{N_t},x_2\right) & \cdots & y\left(t_{N_t},x_m\right)\end{bmatrix}, \tag{7}$$

where $\boldsymbol{y}$ and $\boldsymbol{\Phi}$ represent the acceleration response and its mode of the structure, respectively. $\boldsymbol{\Phi}$ is derived from the canonical orthogonal basis of the eigenvectors $\boldsymbol{\Omega}$ of the covariance matrix $\boldsymbol{Q}$ corresponding to the acceleration response:

$$\boldsymbol{\Phi}=\left\{\boldsymbol{\varphi}_1,\boldsymbol{\varphi}_2,\ldots,\boldsymbol{\varphi}_m\right\}=\left\{\frac{\boldsymbol{\Omega}_1}{\sqrt{\Omega_{12}}},\frac{\boldsymbol{\Omega}_2}{\sqrt{\Omega_{22}}},\ldots,\frac{\boldsymbol{\Omega}_m}{\sqrt{\Omega_{m2}}}\right\}. \tag{8}$$

After the neural network converges, the spatial field of the signal can be reconstructed using the obtained time evolution coefficients as

$$\hat{\boldsymbol{y}}\left(\boldsymbol{x},\boldsymbol{t}\right)=\sum_{i=1}^{N}\sum_{j=1}^{m}\hat{a}_i\left(t\right)\varphi_j\left(x\right)=\begin{bmatrix}\hat{a}_1\left(t\right)\varphi_1\left(x\right) & \hat{a}_1\left(t\right)\varphi_2\left(x\right) & \cdots & \hat{a}_1\left(t\right)\varphi_m\left(x\right)\\ \hat{a}_2\left(t\right)\varphi_1\left(x\right) & \hat{a}_2\left(t\right)\varphi_2\left(x\right) & \cdots & \hat{a}_2\left(t\right)\varphi_m\left(x\right)\\ \vdots & \vdots & \ddots & \vdots\\ \hat{a}_N\left(t\right)\varphi_1\left(x\right) & \hat{a}_N\left(t\right)\varphi_2\left(x\right) & \cdots & \hat{a}_N\left(t\right)\varphi_m\left(x\right)\end{bmatrix}. \tag{9}$$

The accuracy of the POD method in signal reconstruction can be evaluated by comparing the reconstructed signal $\hat{\boldsymbol{y}}\left(\boldsymbol{x},\boldsymbol{t}\right)$ with the filtered signal $\boldsymbol{y}\left(\boldsymbol{x},\boldsymbol{t}\right)$. As eigenvalues decay rapidly, a small number of POD bases often capture sufficient information from the raw data. Consequently, POD analysis based on a limited number of snapshots enables the effective extraction of structural features from complex systems.

The features contained in the first *m* POD bases can be characterised by the generalised ‘energy’, referred to as eigenvalues. And the ‘energy’ proportion represents the proportion of the sum of the eigenvalues of a given order to the sum of all eigenvalues and is defined as

$$\boldsymbol{E}_{\mathrm{POD}}=\frac{\sum_{i=1}^{m}\lambda^{(i)}}{\sum_{j}^{M}\lambda^{(j)}}. \tag{10}$$

Usually, the sequence of eigenvalues $\left\{\lambda^{(1)},\cdots,\lambda^{(m)}\right\}$ decays so fast, and the first few of POD bases contain enough generalised ‘energy’ or structural performance features in the raw data. Therefore, for complex systems, POD analysis based on a certain number of snapshot information helps to extract structural features efficiently.

A series of acceleration responses obtained from accelerometers are used as the network input, which includes both collision and non-collision data. These data are categorised into cases related with the shutdown and different levels of operating conditions. The ‘state label’ is assigned to the samples depending on whether collision occurred between the ship and the wind turbine. Furthermore, the time evolution coefficients $\hat{\boldsymbol{A}}$ and their corresponding values $\hat{\boldsymbol{F}}$ in the frequency domain are extracted from the acceleration response through the POD feature extraction block of the ColliNet architecture. Taking the first *m* orders of the time evolution coefficients, their corresponding values in the frequency domain are calculated using Eq. (11) as follows:

$$\hat{\boldsymbol{F}} = \sum_{n=0}^{N_t-1} \hat{A}\,\omega_{N_t}^{kn} = \sum_{i=1}^{N_t}\sum_{j=1}^{m} \hat{\boldsymbol{F}}_{ij} = \begin{bmatrix} \hat{\boldsymbol{F}}_{11} & \hat{\boldsymbol{F}}_{21} & \cdots & \hat{\boldsymbol{F}}_{N_t 1} \\ \hat{\boldsymbol{F}}_{12} & \hat{\boldsymbol{F}}_{22} & \cdots & \hat{\boldsymbol{F}}_{N_t 2} \\ \vdots & \vdots & \ddots & \vdots \\ \hat{\boldsymbol{F}}_{1\boldsymbol{m}} & \hat{\boldsymbol{F}}_{2\boldsymbol{m}} & \cdots & \hat{\boldsymbol{F}}_{N_t \boldsymbol{m}} \end{bmatrix}, \tag{11}$$

where i denotes the position of the time series of the time evolution coefficients, j represents the spatial index, $A(i)$ signifies the i^{th} order time evolution coefficients extracted from the signal, ω_{N_t} indicates the N^{th} root of unity, commonly represented as e^{-j} in the DFT to compute frequency components, while $\hat{\boldsymbol{F}}_{ij}$ refers to the corresponding item in the frequency domain matrix. The TFF feature vector $\hat{\zeta} = \{\hat{\boldsymbol{A}}, \hat{\boldsymbol{F}}\}$ is used as the input for the second feature processing block so as to realize the classification, as shown in the left part of the BiGRU feature classification block in Fig. 3.

Conventional GRU networks can only encode front-to-back sequence information and are incapable of dealing with back-to-back sequence information. In this study, a Bidirectional GRU network is employed to capture bidirectional structural features. The BiGRU model was first introduced by GrüßerSinopoli and Thalemann (Zhu et al., 2019). The basic unit of the BiGRU model consists of a forward-propagating GRU unit and a backward-propagating GRU unit. Thus, the output layer contains both past and future information. The BiGRU transmission process is formulated as follows:

$$\begin{cases} \vec{h}_t = \mathrm{GRU}(x_t, \overrightarrow{h_{t-1}}) \\ \overleftarrow{h}_t = \mathrm{GRU}(x_t, \overleftarrow{h_{t-1}}) \\ h_t = \omega_t \vec{h}_t + \upsilon_t \overleftarrow{h}_t + b_t, \end{cases} \tag{12}$$

where $\mathrm{GRU}(x_t, \overrightarrow{h_{t-1}})$ and $\mathrm{GRU}(x_t, \overleftarrow{h_{t-1}})$ represent the forward and backward GRU units at time t, respectively. $\vec{h}_t$ and $\overleftarrow{h}_t$ are denoted as the forward and backward transmitted states. ω_t and υ_t mean the weights, and b_t is the bias at time t. A structural overview of the BiGRU network is the right part of the BiGRU feature classification block in Fig. 3.

The TFF feature ζ serves as the input to the second feature processing block that is called BiGRU feature classification block to identify whether collision has occurred. In this network block, the MSE loss is chosen as the loss function:

$$\mathrm{L}_2 = \frac{1}{N}\sum_{i=1}^{N}(y_{pred} - y_{true})^2, \tag{13}$$

where y_{pred} and y_{true} represent the predicted and true values, respectively.

The lower the MSE value, the better the model performance. To address the issue of neuron death arising from the traditional ReLU function when $x < 0$, the LeakyReLU activation function is adopted:

$$h_{\omega}(x_i) = \begin{cases} x, & x > 0 \\ \alpha x, & x \le 0. \end{cases} \tag{14}$$

The loss function evaluates the performance of the ColliNet architecture on the training samples, and the expression for the final loss function over the entire training dataset is given as follows:

$$
\begin{aligned}
\mathrm{L} &= \lambda_1 \mathrm{L}_1 + \lambda_2 \mathrm{L}_2 \\
&= \lambda_1 \left(\lambda_{11} \frac{1}{N} \sum_{n=1}^{N} (\hat{q}_n - q_n)^2 + \lambda_{12} \frac{1}{N} \sum_{n=1}^{N} (\hat{a}_n - a_n)^2 + \lambda_{13} \ell \left\| V \right\|_2^2 \right) \\
&\quad + \lambda_2 \left(\frac{1}{N} \sum_{i=1}^{N} (y_{pred} - y_{true})^2 \right),
\end{aligned} \tag{15}
$$

where λ_1 and λ_2 represent the weight of L_1 and L_2, respectively.

This study proposes an activation function employing a rounding mechanism, designed to map continuous model outputs into discrete collision versus non-collision classification categories. The function is defined as

$$
f(x) = n + \sigma(\tau(x - n - 0.5), \tag{16}
$$

where n represents the integer part of the output x, $\sigma(\cdot)$ denotes the sigmoid function, τ states the temperature coefficient (approximation strictly rounded for $\tau \gg 1$). If $f(x) \geq n + 0.5$, the event is classified as collision; Otherwise, it is classified as non-collision.

To more clearly demonstrate the difference between collision and non-collision, Fig. 5 provides a schematic of collision identification over a one-hour period, with a red line indicating the collision boundary. Values above this threshold fall within the light red ring-shaped area indicating collision, while values below this threshold are classified as non-collision within the remaining area.

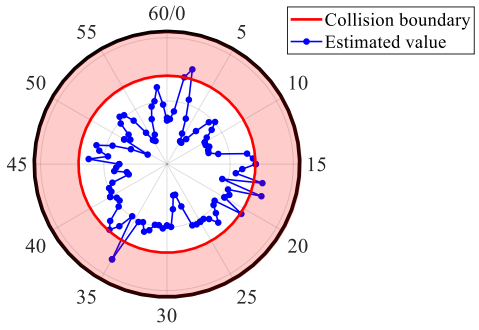

Fig. 5. Schematic diagram of collision identification (Unit: minutes).

Furthermore, Adaptive moment estimation (Adam) is selected as the optimiser in the network training process. Adam is an algorithm for calculating the adaptive learning rate of each parameter, combining the advantages of both AdaGrad and RMSProp. It also enables the smooth update of parameters and works independently without considering the scaling transformation of the gradient. The hyper-parameters used in the network training are shown in Table 1.

Table 1 Hyper-parameters of the ColliNet.

Parameters	Values
Learning rate	0.0001
Training epochs	300
Loss function	MSE
Activation function	LeakyReLU
Batch size	64
Optimiser	Adam

The data collected from numerical simulations or experiments is processed using the same filters and intervals as those in the training process. The data samples are then fed into the trained ColliNet for collision identification. The evaluation index *accuracy* in Eq. (17) is applied to assess the model's

performance, and the higher value of accuracy indicates the better performance of the network (Sei and Ohsuga, 2021):

$$accuracy = \frac{TP + TN}{TP + TN + FP + FN}, \tag{17}$$

where True Positive (TP), True Negative (TN), False Positive (FP), and False Negative (FN) values are elements defined in the confusion matrix. The value of *accuracy* ranges from 0 to 1, with the higher value indicating the greater prediction accuracy.

In summary, the whole process of the proposed ColliNet collision identification architecture is described as follows: (1) Acceleration data pre-processing; (2) POD feature extraction block; (3) Feature fusion and BiGRU feature classification block; (4) Results output. The process can be expressed as shown in Fig. 6.

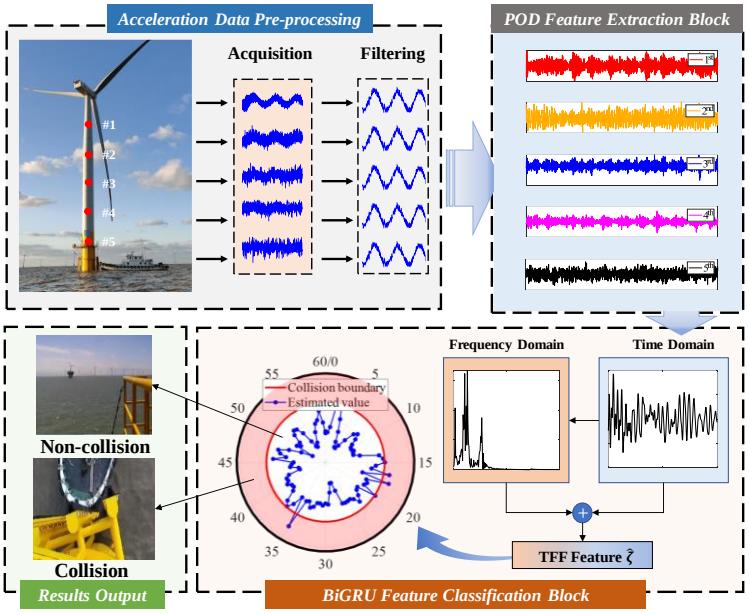

Fig. 6. The process of ColliNet collision identification architecture.

Throughout the above steps, the proposed ColliNet architecture enables the feature extractions from online data autonomously for collision identification after being trained with offline data, and its pseudo code is shown in Algorithm 3.1.

Algorithm 3.1 The ColliNet collision identification algorithm

Input: time series of acceleration response $y(n)$, learning rate α, number of hidden units, number of outputs, layers of BiGRU to stack, number of BiGRU network layers, layer l weight $\boldsymbol{W}^{(l)}$, layer l values $\boldsymbol{a}^{(l)}$, layer l bias $\boldsymbol{b}^{(l)}$

1: Initialise: $\boldsymbol{W}^{(l)} \leftarrow 0$, $\boldsymbol{a}^{(l)} \leftarrow 0$, $\boldsymbol{b}^{(l)} \leftarrow 0$

2: for epoch = 1 ... p

3: for i = 1 ... l-1

4:
$$\begin{aligned} \mathrm{L} &= \lambda_1 \mathrm{L}_1 + \lambda_2 \mathrm{L}_2 \\ &= \lambda_1 \left(\lambda_{11} \frac{1}{N} \sum_{n=1}^{N} (\hat{q}_n - q_n)^2 + \lambda_{12} \frac{1}{N} \sum_{n=1}^{N} (\hat{a}_n - a_n)^2 + \lambda_{13} \ell \left\| V \right\|_2^2 \right) \\ &\quad + \lambda_2 \left(\frac{1}{N} \sum_{i=1}^{N} (y_{pred} - y_{true})^2 \right) \end{aligned}$$ (See Eq. (15) for details)

5: Update layer l weights $\boldsymbol{W}^{(l)}$, layer l bias $\boldsymbol{a}^{(l)}$, layer l bias $\boldsymbol{b}^{(l)}$

6: end

7: end

8: Input features transformed from online real-time data to the trained network to obtain the collision identification results.

Output: identification result y_{pred}

In summary, the advantages of the proposed ColliNet are listed below:

(1) As the raw input signals are first converted into time evolution coefficients in the first feature processing phase, structurally relevant modal information is eliminated, therefore enhancing the ANN generalisation.

(2) The TFF features of the time evolution coefficients are incorporated as inputs to the second feature processing phase called feature classification block, which enhances the robustness of the BiGRU neural network.

4. Validation of ColliNet using simulation data

To validate the effectiveness of the ColliNet architecture proposed in Section 3 and assess its robustness under complex operating conditions, an initial demonstration is first made in this section through numerical simulations. Firstly, the collision module is developed and implemented into OpenFAST to provide a dataset preparation for subsequent network training. Secondly, the physical information in the neural network blocks is revealed to explain the loss functions of each component more precisely. Finally, the efficiency of the proposed collision identification architecture is verified using OpenFAST numerical simulation data.

4.1 OpenFAST simulation dataset preparation

The NREL offshore 5-MW baseline wind turbine is selected as the benchmark model for this study, which has been widely adopted to establish standard offshore wind turbine specifications and to quantify the benefits of advanced wind energy technologies in many research studies (Lindenburg and Winkelaar, 2003). The monopile type is chosen for the specific study, which represents the fundamental and commonly used configuration in offshore wind turbines. The detailed parameters of the model are presented in Table 2.

Table 2 Parameters of the NREL 5-MW monopile wind turbine (Jonkman et al., 2009).

Positions	Parameters	Values	Unit
Gross properties	Rotor diameter	126	m
	Hub height	90	m
	Cut-in, rated, cut-out wind speed	3, 11.4, 25	m/s
	Cut-in, rated rotor speed	6.9, 12.1	rpm
Blade	Length	61.5	m
	Mass	17740	kg
	1st edgewise mode natural frequency	1.08	Hz
	1st flapwise mode natural frequency	0.68	Hz
Nacelle + hub	Nacelle mass	240000	kg
	Hub mass	56780	kg
	Hub diameter	3	m
Tower	Mass	346460	kg
	Height above ground	87.6	m

Though commercial finite element analysis tools such as ANSYS and LS-DYNA excel at simulating collisions and interactions of complex structures, they all assume the blades remain stationary during simulations, limiting the application of wind turbines to the analysis under a shutdown condition only. On the contrary, OpenFAST is specifically designed for the dynamic simulation of wind turbines, enabling precise parametric modelling under the consideration of the rotation speed, pitch angle, and other factors to realize various operating conditions. This advantage makes it more suitable for simulation with interactions between wind turbines and their environments. Therefore, the 5-MW monopile wind turbine in this study is analysed by OpenFAST.

OpenFAST models the wind turbine as a multi-body system using the Kane method (Lee et al., 2002; Sarkar and Fitzgerald, 2020). In particular, the Kane's equations of motion for a complete system of wind turbines with r degrees of freedom are as follows (Sarkar and Fitzgerald, 2021) :

$$\hat{F}_r^* + \hat{F}_r = 0, \tag{18}$$

where $\hat{F}_r^*$ and $\hat{F}_r$ are the generalised active and the generalised inertia forces respectively.

Moreover, considering the collision loads, the of motion equation of the wind turbine is expressed as

$$\begin{cases} \hat{F}_r^* + \hat{F}_r\big|_{AF} + \hat{F}_r\big|_{GF} + \hat{F}_r\big|_{EF} + \hat{F}_r\big|_{DF} + \hat{F}_r\big|_{HF} + \hat{F}_r\big|_{GE} + \hat{F}_r\big|_{CF} = 0 \\ \hat{F}_r\big|_{CF} = E_{v_r}^{\mathrm{T}} \{P(t)\}, \end{cases} \tag{19}$$

where $\hat{F}_r\big|_{AF}$, $\hat{F}_r\big|_{GF}$, $\hat{F}_r\big|_{EF}$, $\hat{F}_r\big|_{DF}$, $\hat{F}_r\big|_{HF}$, $\hat{F}_r\big|_{GE}$, and $\hat{F}_r\big|_{CF}$ represent the generalised aerodynamic, gravitational, elastic, damping, hydrodynamic and motor transmission, collision forces of the modified model, respectively. $E_{v_r}^{\mathrm{T}}$ indicates the partial linear velocity of the wind turbine tower at the r^{th} degree of freedom.

The collision between a ship and an offshore structure can be simplified as an isosceles triangle with a collision load $P(t)$ applied on one end of a nonlinear spring (Jin et al., 2005), while the other end of the spring is connected to the impacted member of the offshore structure, as shown in Eq. (20). A 5-MW monopile wind turbine visualised in ParaView combined with the simplified loads is shown in Fig. 7 (a). For multiple collisions with period T, the time history of the collision load $P(t)$ is depicted in Fig. 7 (b).

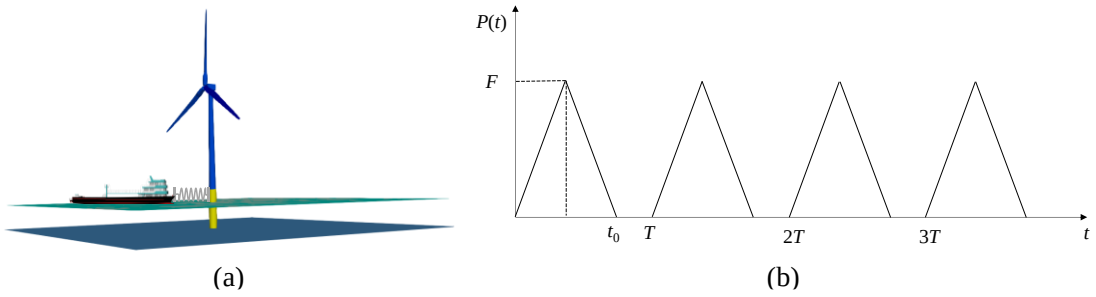

(a) (b)

Fig. 7. The 5-MW monopile wind turbine model in OpenFAST and its simplified collision load history. (a) The wind turbine model; (b) Periodic loads from multiple collisions.

$$P(t) = \begin{cases} 2Ft/t_0, & 0 \ \ t \ \ t_0/2 \\ 2F\left(1 - t/t_0\right), & t_0/2 \ \ t \ \ t_0 \\ 0, & t_0 \ \ T \end{cases} \tag{20}$$

The magnitude of the maximum collision load F is derived from an empirical formula, which is defined in the General Specifications for Design of Highway Bridges and Culverts (China, 2015):

$$F = \frac{WV_0}{g\,t}, \tag{21}$$

where W denotes the ship's mass, V_0 represents the collision velocity, g indicates the gravitational acceleration, and t stands for the duration of the impact and typically is set to 1s in the absence of specific data. The structural parameters for the ship-turbine collision module are listed in Table 3.

Table 3 Structural parameters for the ship-turbine collision module.

Structural parameters	Values	Unit
Mass density	700	kg/m^3
Poisson's ratio	0.3	/
Wedge angle	90	degree
Young's modulus	200	GPa

The development of the collision module is inspired by Sub-Model 2 of Ice Model 1 in the IceDyn Model (Dale and Bingbin, 2015). Firstly, an elastic wedge is assumed to float on an elastic foundation under load, and the corresponding simplified collision forces can be obtained based on collision velocities and ship masses common in engineering practice. Then, this relationship is written into a file of type *sln* to form a custom collision module. Finally, the file is recompiled to integrate the module into OpenFAST.

After the collision module has been implemented into OpenFAST, it is necessary to set the values of input parameters reflecting the actual engineering conditions for accurate simulation of the collision process between the ship and the wind turbine. To more exactly simulate the randomness of collisions in practice as well as the non-uniformity of the ship's parameters such as mass and velocity, the loads considered in this study are non-periodic random with different intervals between successive collisions and non-uniform magnitude. Approximately 95% of offshore wind turbine collisions occurred with service ships (DNVGL, 2015), therefore service ships are considered as the main type in this study. Furthermore, Bela et al. (2017) indicated that the maximum collision velocity which a wind turbine on a monopile foundation can withstand is 3 m/s, considering the seabed soil conditions. Approximately 20% of these collisions are head-on impacts, which typically occur at velocities between 1.3 m/s and 3.0 m/s due to insufficient braking. The remaining 80% are drift collisions and typically are identified at velocities ranging from 0.3 m/s to 2.2 m/s. This is driven by sea winds and waves during ship collisions. Therefore, the wave in the shutdown condition is also considered as a variable parameter. Moreover, service ships vary in mass from approximately 1000 to 4000 tons depending on their functionality (Ellinas, 1995).

Apart from the collision velocity and the mass of the ship, the wind speed also significantly affects the structural response. Based on the cut-in, rated, and cut-out wind speeds provided in Table 2, the wind speed range in this study spans from 1 m/s to 25 m/s. This covers the entire range of turbine operations from shutdown condition to full power generation, and then the shutdown again due to the cut-out wind speeds. In summary, the simulations of ship-wind turbine collision are considered using the add-on module implemented into OpenFAST with the consideration of different wind speeds, ship masses, and collision velocities to ensure the integrity of each dataset. A total of 500 working conditions are designed for simulation, with specific conditions outlined in Table 4. As depicted in Fig. 8, the maximum structural acceleration of wind turbines under different collision velocities and ship masses is analysed. The results indicate that the structural response intensifies with an increase in either ship mass or collision velocity. Specifically, the acceleration exhibits a non-linear growth trend, with a minimum value of 0.069 g and a maximum of about 12.5g, which demonstrates that the energy generated by the impact during the ship collision has a significant effect on the wind turbine structure. By coupling the effects of ship mass and

collision velocity, the simulation process provides a comprehensive understanding of the dynamic behaviour of wind turbines in operational and extreme conditions.

Table 4 Arrangement of OpenFAST simulation conditions.

	Collision			Non-collision	
Working condition	Collision velocity (m/s)	Ship mass (tons)	Wind speed (m/s)	Wind speed (m/s)	Wave or not
Shutdown	0.1 0.5-3 (Interval of 0.5)	1000-4000 (Interval of 1000)	1	1	Yes No
Normal Operation	0.1 0.5-3 (Interval of 0.5)	1000-4000 (Interval of 1000)	3-25 (Interval of 2)	3-25 (Interval of 0.5)	Yes

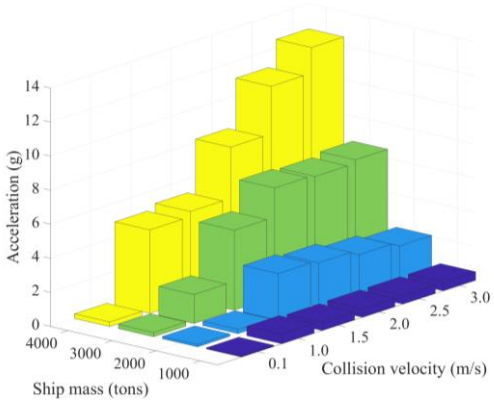

Fig. 8. Maximum values of structural acceleration of wind turbines for different collision speeds and ship masses at the rated wind speed of 11.4 m/s**.**

4.2 Physical information of the POD feature extraction block

In this subsection, the physical information embedded in the first feature processing phase, that is called POD feature extraction block, will be elucidated, which includes the obtaining of the true value of time evolution coefficients $\boldsymbol{A}$ and the reconstruction of the acceleration responses.

Since the ship collision usually occurs at the lower part of the wind turbine tower and closes to the base flange. Hence the acceleration response at the 5^{th} measurement point closest to the water surface is chosen as the representative data. A typical non-collision segment of acceleration responses and three segments with different collision intensities are selected for the comparative study, as depicted in Fig. 9. The sampling frequency is 200 Hz, with each segment spanning of 10 s. Fig. 9 (a) shows the raw non-collision and collision acceleration time histories in the x-direction, while Fig. 9 (b) illustrates the corresponding power spectral densities.

As can be observed in Fig. 9, the amplitude of the acceleration in the non-collision condition is an order of magnitude smaller than that in the minor collision. Under the non-collision condition, the structure is mainly affected by incoming currents, waves, and rotor blade rotation, with the main vibration frequency at 0.3 Hz, which is close to the first-order natural frequency of the structure. During the minor collision, the dominant vibration frequency shifts to 2.3 Hz, and as the collision severity increases, higher-order frequencies become more prominent, with the dominant frequency reaching 5.3 Hz in severe collision. The power spectral density amplitude is significantly larger under collision conditions due to the new energy introduced by the ship impact. The time-domain signals are affected by noise and environmental variations, causing irregularities, whereas the frequency-domain signals are smoother and less susceptible to these disturbances, and this stability can enhance the neural network's ability to

achieve superior learning and generalisation. In Addition, the frequency domain representation more effectively captures the periodicity and harmonic characteristics of the signals, which are critical for pattern identification and feature extraction in neural networks. Therefore, both time and frequency domain information will be incorporated into the subsequent collision identification architecture.

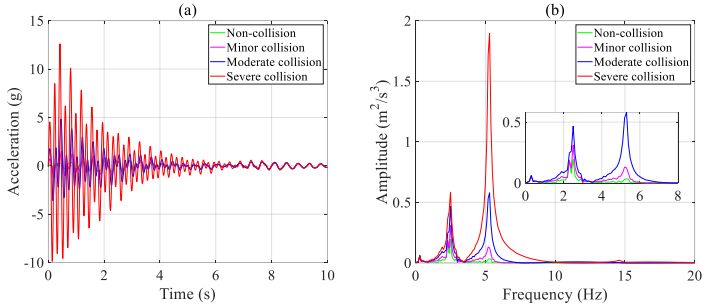

Fig. 9. Raw acceleration signal and corresponding power spectral densities: (a) The time history of acceleration signals; (b) Power spectral densities corresponding to the acceleration signals.

To facilitate a comprehensive analysis of the signal components associated with ship-wind turbine collision events, the raw acceleration signals of the wind turbine need to be pre-processed. It is critical as collision signals are often obscured by background noise and uncorrelated high-frequency components. A DFT-based filtering method is employed, aiming at eliminating these interferences while preserving frequency components below 20 Hz, which typically encapsulate vital dynamic information pertinent to the ship collision. This filtering process not only mitigates extraneous noise but also smooths out fluctuations in the raw data, thus capturing the transient features of the collision. Therefore, the filtered signals will form the basis for future investigations aimed at better identifying the ship collision.

Moreover, the spatial modes $\boldsymbol{\Phi}$ of the structure and their corresponding time evolution coefficients $\boldsymbol{A}$ can be obtained according to Eqs. (7) and (8). The time coefficients $\boldsymbol{A}$ are independent of the structure itself, thus reducing the spatial complexity of the data. In signal processing and vibration analysis, the square of the signal amplitude represents instantaneous power, while its accumulation denotes total energy, reflecting the signal's intensity (Chen et al., 2000). While in POD analysis, the generalised energy distribution i.e., the percentage of generalised energy associated with each orthogonal basis vector, is of primary interest. According to Eq. (10), the proportion of the first L orthogonal basis vectors in the total energy is determined by calculating the proportion of the sum of the first L eigenvalues to the sum of the total eigenvalues, allowing the optimal number of orthogonal dimensions to be selected. In the OpenFAST simulation, the five measurement points set up are positioned along the axial direction of the wind turbine tower to maximise the generalised energy proportions and cumulative proportions corresponding to the first five orders of the basis. It is found from Fig. 10 that both non-collision and collision conditions are dominated by a single mode, accounting for over 60% of the total energy. As the intensity of the collision increases, higher order frequencies dominate. In moderate collision, a modal shift occurs and the first-order dominant energy decreases to around 64%.

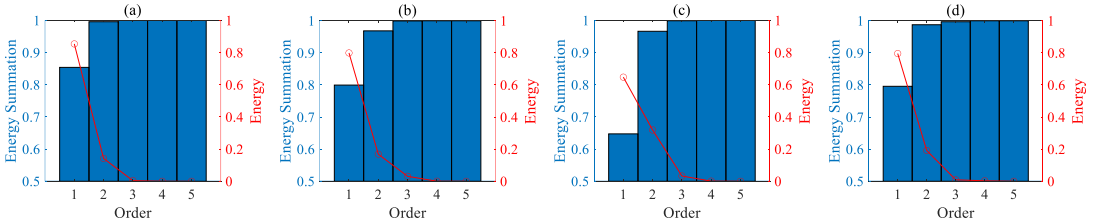

Fig. 10. Generalised energy distribution of the acceleration responses: (a) Non-collision; (b) Minor collision; (c) Moderate collision; (d) Severe collision.

The time histories of the time evolution coefficients $\boldsymbol{A}$ for the first five orders of the acceleration signals are presented in Fig. 11, where a gradual decrease in amplitude of the time evolution coefficients from the first to the fifth order modes is observed. This aligns with the proportions of the generalised energy. Fig. 12 illustrates the reconstructed acceleration responses utilising these coefficients according to Eq. (9). By calculating the difference between the reconstructed and actual values, it can be found that the residuals range from [-1.5e-16, 2e-16] for the non-collision condition to [-4e-14, 4e-14] for the severe collision condition. Hence, one can conclude that the parameters extracted by the POD method effectively reconstruct the acceleration responses of the structure. Moreover, the time evolution coefficients are dimensionless parameters that provide a more generalised representation compared to the raw acceleration signals, thereby enhancing the applicability and generality of the results. Therefore, in the subsequent neural network training, these time evolution coefficients will be employed as the true values for the first feature processing phase called POD feature extraction block, and the predicted time evolution coefficients will be trained as the input parameters for the second feature processing phase called BiGRU feature classification block to improve model accuracy and generalisation.

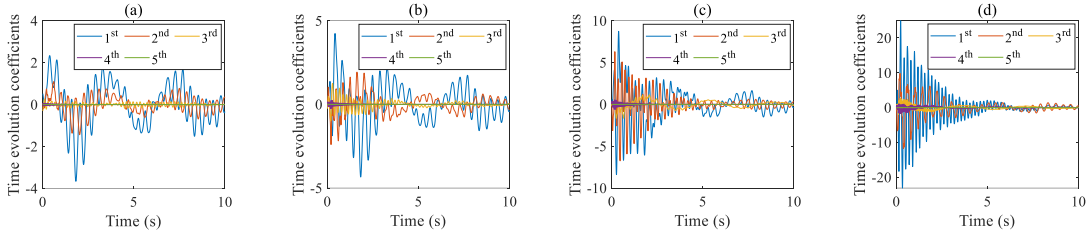

Fig. 11. The first five orders of time evolution coefficients versus time: (a) Non-collision; (b) Minor collision; (c) Moderate collision; (d) Severe collision.

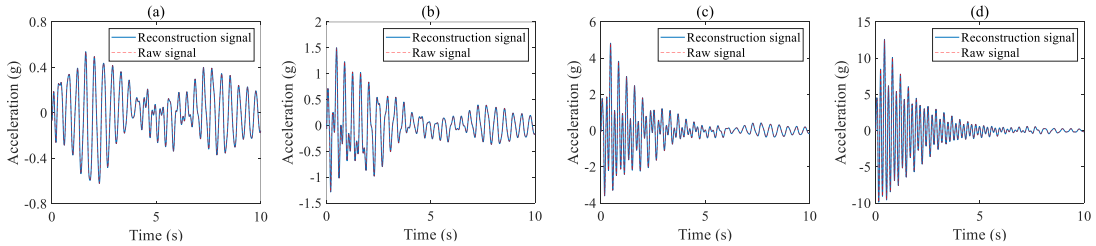

Fig. 12. Comparison of reconstructed and raw signals: (a) Non-collision; (b) Minor collision; (c) Moderate collision; (d) Severe collision.

4.3 Results of the proposed ColliNet architecture

As described in Section 3, the ColliNet architecture includes the following steps to realize the collision. The filtered acceleration response is fed into the network, which is first trained by the POD feature extraction block that is constrained using the loss function in Eq. (6) to predict the time evolution coefficients $\boldsymbol{A}$. Secondly, the frequency domain values $\boldsymbol{F}$ of the time evolution coefficients $\boldsymbol{A}$ are derived from their time domain values by employing the DFT method and fused with the time domain values to obtain the TFF features $\boldsymbol{\zeta}$. Subsequently, the next feature processing phase, namely the BiGRU feature classification block, is entered for further capturing the potential collision features of the signals. Finally, a fully connected layer is utilised to reduce the dimensionality of the parameters and obtain classification results.

The network is trained using 500 data sets generated from OpenFAST numerical simulations, comprising 350 collision data sets and 150 non-collision data sets, as detailed in Table 4. The acceleration responses from the five measurement points served as network inputs. The distribution of the datasets is partitioned into training (60%), validation (20%), and testing (20%) sets. The input layer dimensions are configured to 10×2000, while the hidden layer dimensions are set to 1×300, and the output dimension is established as 1×1. The MSE loss function and Adam optimiser are employed with a learning rate of

1×10^{-4} and a batch size of 64. Results of true and predicted values across the training, validation and testing stages are depicted in Fig. 13. To enhance clarity and intuitiveness in illustrating identification performance across different working conditions, a polar coordinate representation is employed. In the figures, the red points signify true values, while the green points signify predicted values, with the points at identical angles corresponding to the same set of data. All the points situated within the light red ring-shaped area indicate collision, whereas the points within the remaining area indicate non-collision. It is evident that a majority of green and red points positioned at the identical angles are situated within the same colour area and are in close proximity to each other, which indicates that the model predicted values are highly consistent with the true values, qualitatively demonstrating the accuracy of the architecture. Quantitatively, the ColliNet architecture demonstrates exceptional performance in identifying the collision and non-collision conditions between ships and wind turbines. Specifically, the accuracy of the training, validation and testing sets reaches 99.67%, 99% and 100%, respectively. These results not only confirm the effectiveness of the ColliNet architecture in the training stage, but also demonstrate its consistently high accuracy in the validation and testing stages.

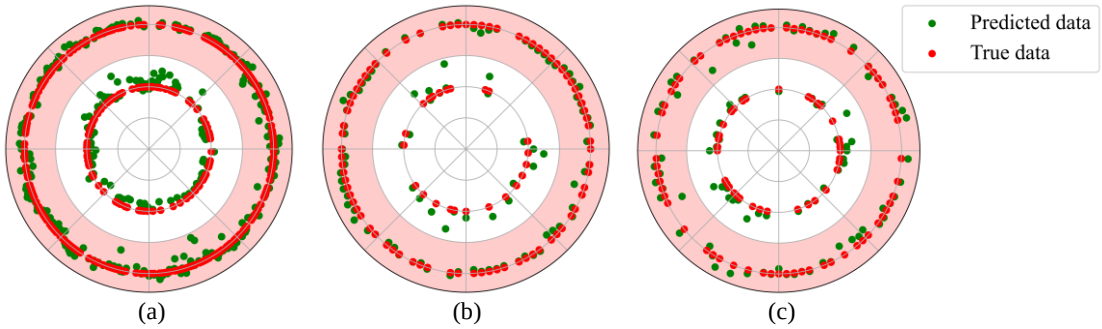

Fig. 13. Comparison of predicted and true results with OpenFAST dataset. A pair of red and green points at same radiated line corresponds to the same load condition: (a) Training results; (b) Validation results; (c) Testing results.

To evaluate the enhancement of the ColliNet architecture, four comparative models are tested, including the BiGRU feature classification block separately, the frequency domain enhanced BiGRU feature classification block (FE-BiGRU), the BiGRU feature classification block combined with POD feature extraction block (POD-BiGRU), and the BiGRU feature classification block with the frequency domain enhanced POD feature extraction block (FE-POD-BiGRU). LSTM and CNN based methods are used for comparison to better demonstrate the superiority of the method. The average accuracies are computed after five sessions for each model, with results presented in Table 5. In addition, histograms illustrating the accuracy across the three stages are provided in Fig 14 (a) for enhanced visualisation. The average values of the accuracy of each model at the three stages are also given as a line diagram and star markers in the figure. All computational efficiency evaluations are conducted using the same GPU (NVIDIA GeForce RTX 4070Ti). Analysis of the results of the models for the five configurations revealed that the testing accuracy without POD feature extraction and frequency domain information is 94%; incorporating frequency domain information increased the testing accuracy to 96%; when employing the frequency domain enhanced POD feature for training, the testing accuracy reached 97%; and finally, the testing accuracy reaches 100% after the training with the proposed ColliNet architecture in this paper. Compared with the LSTM and CNN based identification methods, the prediction points of the proposed architecture are more concentrated around the true values, and the accuracy in the testing stage is improved by 7%-8%. The average values of the accuracy of the ColliNet architecture are also much higher than the other methods, which proves the stability of the proposed architecture. Consequently, the enhancement in the accuracy of the proposed architecture is quantitatively confirmed.

In addition, the confusion matrices of the different methods under the testing stage are added, as shown in Fig 14 (b), where the coordinates are 0 for no collision and 1 for collision. It can be found that only in the proposed ColliNet the results are *TP*=65, *TN*=35, *FP*=0, *FN*=0. It proves that the proposed method achieves 100% accuracy in the testing stage. In terms of calculation time, the shortest single testing time for the four models with different configurations is 0.0002 s and the longest is 0.0014 s, both of which meet the requirements for practical applications.

Table 5 Accuracies of the models by different methods.

	Training accuracy (%)	Validation accuracy (%)	Testing accuracy (%)	Testing time (s)
ColliNet	99.67	99	100	0.0014
BiGRU	93.67	93	94	0.0002
FE-BiGRU	99	97	96	0.0002
POD-BiGRU	97.67	97	98	0.0014
FE-POD-BiGRU	99.67	98	97	0.0015
LSTM	96	97	92	0.0003
CNN	95.67	96	93	0.0003

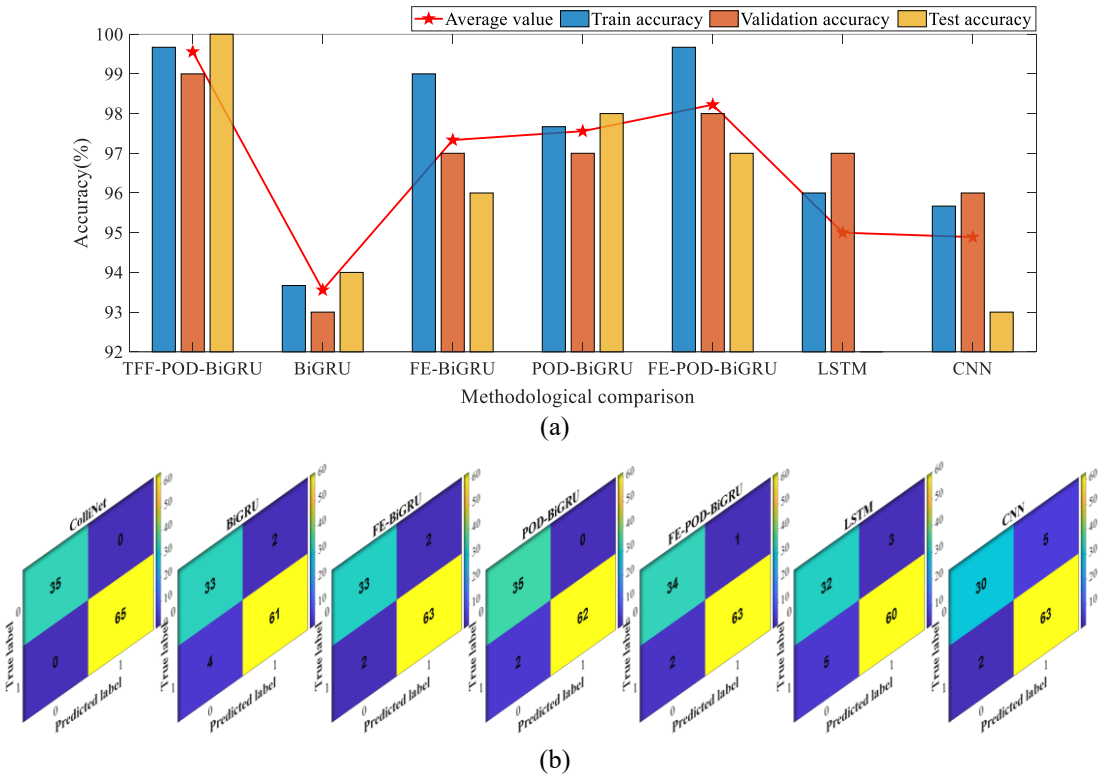

Fig 14. Comparative performance analysis of different methods trained using OpenFAST simulation dataset. (a) Accuracies; (b) Confusion matrices in testing stage.

5. Validation of ColliNet using lab-scale test data

To further validate the accuracy and robustness of the ColliNet architecture for collision identification in practical scenarios, laboratory tests are conducted on a wind turbine model. The external structural dimensions of the tested offshore wind turbine are also based on the NREL 5-MW monopile wind turbine, which is designed and machined according to 1:70 isotropic dimensions, as detailed in Table 6. Five acceleration sensors are installed along the vertical axis (x-direction) of the model, with the y-direction aligned to the primary vibration direction of the shaker, and the z-direction defined as the

tangent direction perpendicular to the main vibration axis. The sensors are located as illustrated in Fig. 15(a).

Table 6 Dimension of components of test wind turbine.

System parameters	Actual value	Unit
Scale ratio	1:70	-
Test model height	120	cm
Diameter of top and bottom	5, 10	cm
Tower wall thickness	0.8	mm
Monopile foundation height	90	cm

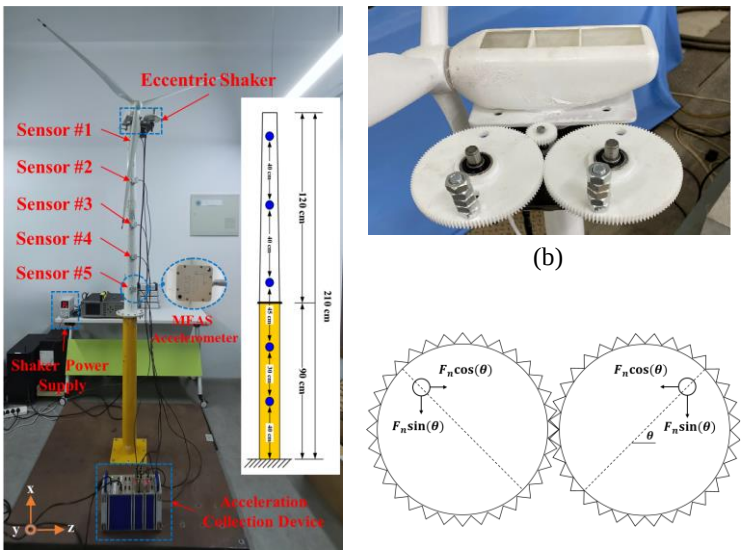

(a) (b) (c)

Fig. 15. Lab-scale collision tests: (a) Test wind turbine model; (b) The detail of the eccentric shaker loading device; (c) The principle of the eccentric shaker loading device.

The operating loads generated by the rotating blades of a wind turbine are simulated using an eccentric exciter. The speed of the exciter is controlled by an adjustable power supply with a voltage range of 4-8 V, corresponding to rotation speeds of 360-1800 rad/min. The operating principle of the eccentric vibrator involves generating a centrifugal force F_n by rotating a mass block on the loading gear via a motor, thereby inducing a sinusoidal cyclic load on the structure. The eccentric shaker loading device and its principle are depicted in Fig. 15 (b) and (c), with the load amplitude defined as:

$$\begin{cases} F_n = mr\omega^2 \\ F_y = 2mr\omega^2 sin(\theta) = 2mr\omega^2 sin(\omega t), \end{cases} \tag{22}$$

where m denotes the mass added to the loading device, r represents the distance from the mass block to the pile body, and ω refers the angular velocity of the gear in a uniform circular motion.

The amplitude and frequency of the applied load are adjusted by regulating the voltage in the device. The test comprises three sets under different excitation loads: no-speed, constant-speed, and variable-speed tests. Specifically, three rotation speeds are set at constant speeds of 360, 1200, and 1800 rad/min, respectively, and the duration of data acquisition is 10 minutes for each condition. The working conditions are summarised in Table 7. Given that most ship collision in practical engineering occur near the base flange, the excitation position is located near Sensor #5, with the excitation direction aligned with the y-axis of the sensor. The excitation is distributed across all specified working conditions. The

acquired acceleration responses are illustrated as blue lines in Fig. 16, with responses from Sensor #1 to Sensor #5 arranged from top to bottom. Collision and non-collision responses are highlighted as red and black lines in the two right-hand columns, respectively.

Table 7 Arrangement of test conditions.

Operating Condition	No Rotation Speed	**Constant Rotation Speed**			Variable Rotation Speed (360-1800 rad/min)
		Rotation Speed 1 (360 rad/min)	Rotation Speed 2 (1200 rad/min)	Rotation Speed 3 (1800 rad/min)	
Acquisition time	10 min	10min	10 min	10 min	10 min

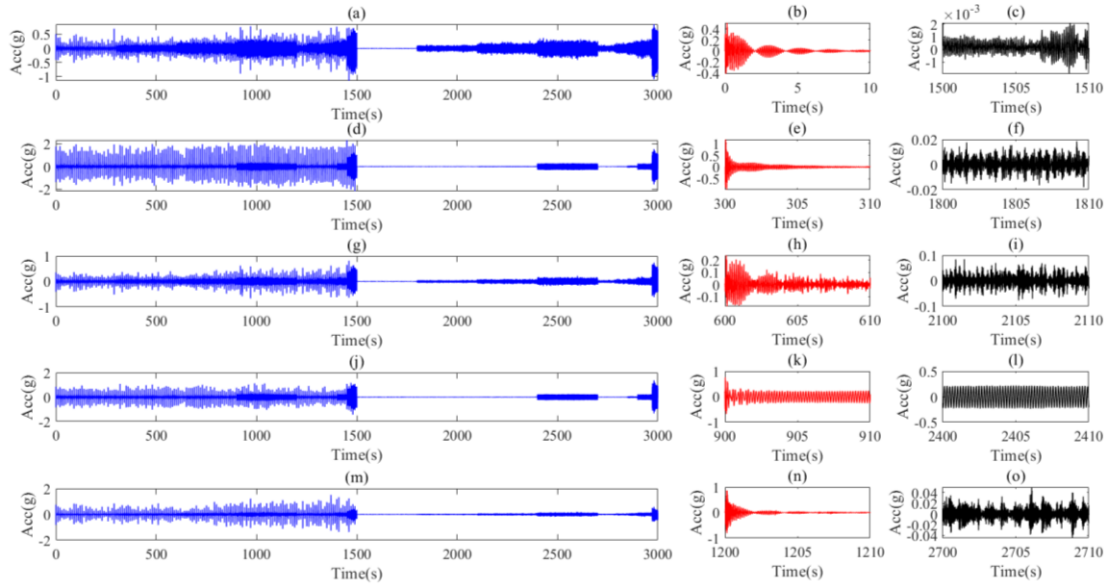

Fig. 16. Acceleration responses of wind turbine tower versus time for lab-scale collision tests (The first column represents the entire data in 3000 s, the second column shows five groups of collision data, and the third column illustrates five groups of non-collision data).

Since the five measurement points are arranged along the axial direction of the wind turbine tower and considering the spatiality of the signal, the first five orders of the time evolution coefficients $\boldsymbol{A}$ of the signals are extracted using the POD method according to Eq. (7). The first five orders of the energy and their cumulative energy sums are shown in Figs. 17 and 18. The first-order energy accounted for a significant proportion of the total energy in all conditions, exceeding 70%. The energy proportion in the collision conditions are relatively uniform, with first-order energy ranging from 70% to 85%, while the first two orders accounted for nearly 100% of the total energy. In non-collision conditions, energy proportion fluctuated based on wind turbine operation; at minimum rotation speed, the first four orders of energy contributed only 98%, whereas at maximum rotation speed, the first-order energy proportion reached 99.5%. The first five orders of time evolution coefficients $\boldsymbol{A}$ at the maximum rotation speed during test are presented in Fig. 19. The amplitudes of the order components of the time evolution coefficients $\boldsymbol{A}$ are positively correlated with energy values across different orders, with a tendency to decrease with increasing order. It is noteworthy that the amplitudes of the first-order time evolution coefficient $\boldsymbol{A}$ in Fig. 19 (b) significantly exceed that of the other orders in the non-collision conditions at the maximum rotation speed.

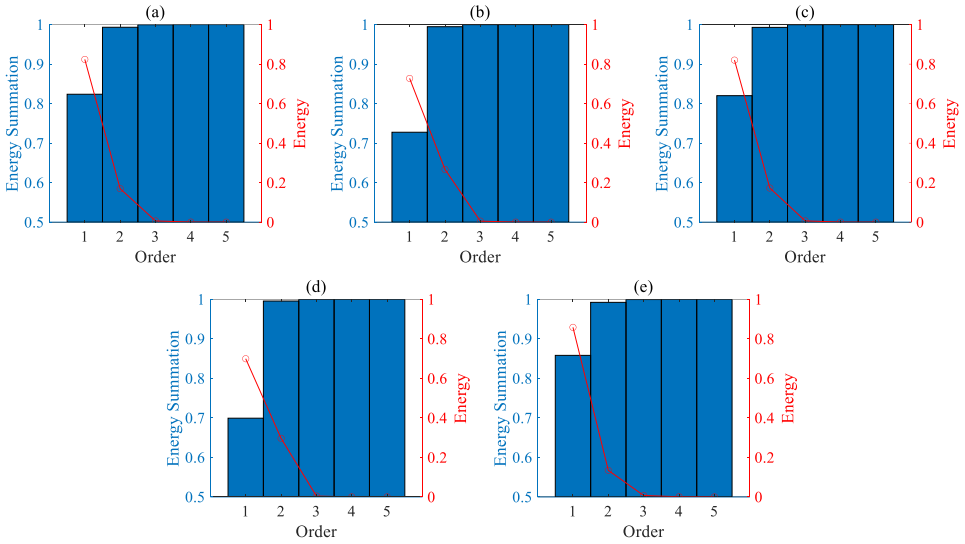

Fig. 17. Energy distribution of the acceleration responses in collision conditions:(a) No rotation speed; (b) Rotation speed 1; (c) Rotation speed 2; (d) Rotation speed 3; (e) Variable rotation speed.

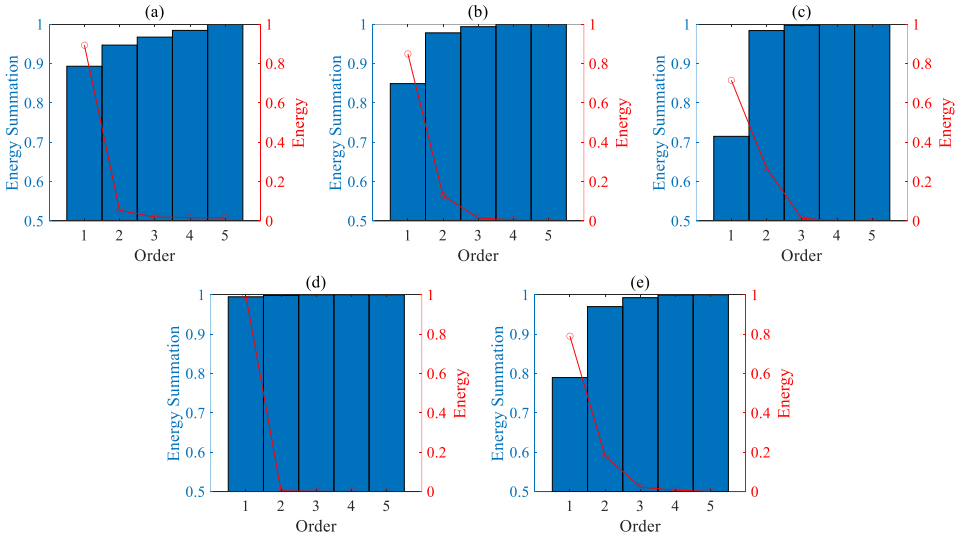

Fig. 18. Energy distribution of the acceleration responses in non-collision conditions:(a) No rotation speed; (b) Rotation speed 1; (c) Rotation speed 2; (d) Rotation speed 3; (e) Variable rotation speed.

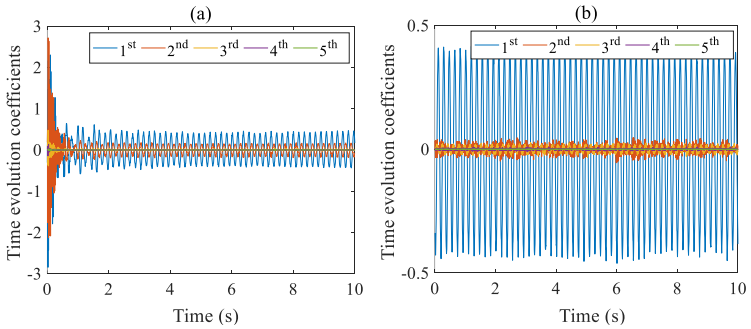

Fig. 19. The first five orders of time evolution coefficients versus time at Rotation speed 3: (a) Collision condition; (b) Non-collision condition.

The first five orders of time evolution coefficients $\boldsymbol{A}$ can be employed to reconstruct the acceleration responses to demonstrate the accuracy of the obtained parameters according to Eq. (7). The residual values between the reconstructed and raw signals fall within the range of [-2e-16, 2e-16] for non-collision conditions and [-1e-15, 1e-15] for collision conditions. Therefore, the acceleration response under lab-scale tests can also be well reconstructed by the time evolution coefficients. These time

evolution coefficients $\boldsymbol{A}$ are used as the true values of the POD feature extraction block, which form the loss function L_1 with the other components as shown in Eq. (6), which co-constrain this network block. Moreover, the TFF features ζ are fed into the BiGRU feature classification block to finalise the collision identification.

As shown in Table 7, a total of 300 sets of tests are conducted, including various operating conditions for the wind turbine at shutdown and different rotation speeds. Collision and non-collision data constituted 50% each of the total dataset. The proportions of the training, validation, and testing sets are also allocated at 60%, 20%, and 20%, respectively. The datasets are shuffled to ensure all working conditions are represented across all stages. The network architecture, layer dimensions, and hyperparameters are consistent with those outlined in Section 4.3. The training process consists of 300 epochs, and the predicted and true values during the training, validation, and testing stages are presented in Fig. 20. The red points represent the true values, while the green points indicate the predicted values, with the identical angular values corresponding to the same data set. The points within the light red ring-shaped area indicate collision, whereas those within the remaining area indicate non-collision. As can be seen from the figure, most of the point pairs from the same dataset are closely located and falling within the same colour area, which qualitatively confirms the validity and stability of the proposed architecture in testing acceleration signals.

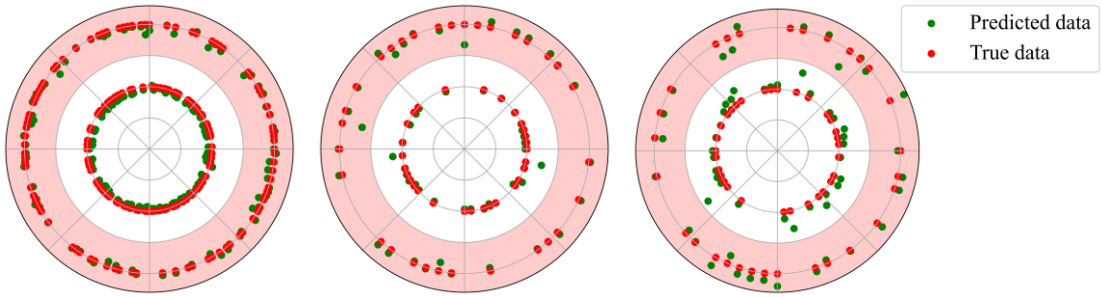

Fig. 20. Comparison of predicted and true results with lab-scale test dataset. A pair of red and green points at same angle corresponds to the same load condition: (a) Training results; (b) Validation results; (c) Testing results.

Similarly, four additional comparison models are employed to evaluate the accuracy enhancement of the ColliNet architecture. The average results after five sessions for each model are shown in Table 8, and the corresponding histograms are illustrated in Fig. 21(a). The average values of the accuracy of the different models under the three stages are indicated by a line diagram and star markers in the figure. Comparison of the results of the five models revealed significant differences. The testing accuracy reaches 93.33% without the POD feature extraction or frequency domain transformation (BiGRU separately). Upon incorporating frequency domain feature (FE-BiGRU), the testing accuracy improved to 98.33%. The test accuracies with POD-BiGRU and FE-POD-BiGRU are both 95%. The average value of the accuracy of the ColliNet architecture is also significantly larger than that of the other models. These results further quantitatively confirm the high accuracy of the proposed architecture in this study. The confusion matrices for the different methods under the testing stage are also given in Fig. 21 (b). Similar to the results for the OpenFAST dataset, the lab-scale test dataset also has only *FP* and *FN* of 0 under the ColliNet architecture in the first image in Fig. 21 (b), which as well confirms that the testing accuracy is 100%. In terms of testing times, the shortest testing time for a single epoch across different methods is 0.0002 s and the longest is 0.0024 s, both of which also meet the requirements for practical application.

Table 8 Accuracies of the models by different methods.

	Training accuracy (%)	Validation accuracy (%)	Testing accuracy (%)	Testing time (s)
ColliNet	100	100	100	0.0018
BiGRU	100	91.67	93.33	0.0003
FE-BiGRU	100	100	98.33	0.0002
POD-BiGRU	100	91.67	95	0.0017
FE-POD-BiGRU	100	100	95	0.0024
LSTM	93.48	86.66	87.22	0.0002
CNN	97	98	94.44	0.0002

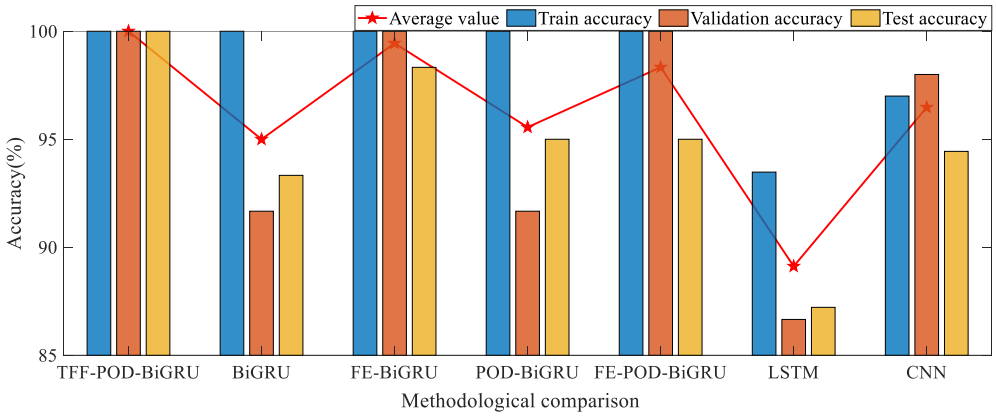

(a)

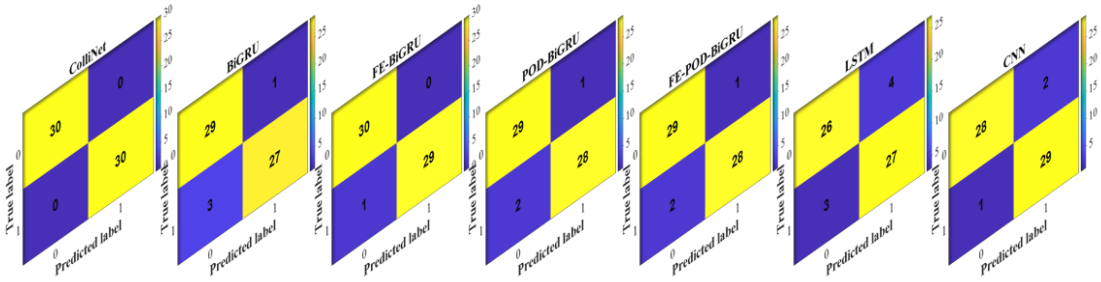

(b)

Fig. 21. Comparative performance analysis of different methods trained using lab-scale test dataset. (a) Accuracies; (b) Confusion matrices in testing stage.

6. Conclusions

This paper proposes a ColliNet network architecture aiming at identifying the collision between ships and wind turbines. Three key contributions are developed for enabling the ship-turbine collision in OpenFAST and enhancing the feature representation and robustness of ColliNet for the collision identification accuracy: 1) An add-on module is implemented into OpenFAST to enable the simulation of collisions between ships and wind turbines at different rotation speeds; 2) A POD feature extraction block is introduced, which effectively captures critical features of time evolution coefficients, thereby enhancing the network's ability to handle complex signals; 3) Time and frequency domain information are fused to significantly improve the pattern identification and feature extraction capabilities of the network architecture, and the TFF features are served as the inputs to the BiGRU feature classification block for supervised training. The accuracy of the proposed ColliNet architecture is verified through OpenFAST simulations and lab-scale test data, which successfully demonstrate the collision identification using the limited sampling data. The implementation of the TFF-POD in ColliNet secures the accuracy increase of collisions from 93.33%-94% to 100%. These results substantially improve the

efficiency of collision identification in autonomous monitoring and provide a reliable guarantee for the safe operation of the offshore wind turbines. With the help of real-time monitoring and data analysis, potential structural damage risks are identified in time for early warning, providing a scientific basis for the maintenance and repair of wind turbine structures.

The present study is our initial exploration into the analysis of ship-wind turbine collisions in offshore engineering, focusing primarily on establishing fundamental correlations through variations in ship mass and collision velocity. The proposed architecture has some limitations including the dependence on the idealized training data and the lack of the generalizability to multiple collision scenarios. The future work will incorporate complex operational parameters, including the collision angle and ship type, while improving the methodology through noise-augmented datasets, lightweight model compression for neural architecture, and spatio-temporal graphical networks to increase the working efficiency when deployed in real-world scenarios. Furthermore, collision positioning studies will be expanded, with an emphasis on quantifying the impact of collisions on wind turbine structures to improve early warning accuracy. This will require a detailed analysis of post-collision structural responses, encompassing material mechanics and structural dynamics, to develop an accurate assessment model.

Declaration of competing interest

The authors declare that they have no known competing financial interests or personal relationships that could have appeared to influence the work reported in this paper.

Acknowledge

The authors acknowledge the financial support from the National Outstanding Youth Science Fund Project of the National Natural Science Foundation of China (52125106) and the National Natural Science Foundation of China (U22A20243).

References

Bela, A., Le Sourne, H., Buldgen, L., Rigo, P., 2017. Ship Collision Analysis on Offshore Wind Turbine Monopile Foundations. Marine Structures. 51, 220-241.

Brighenti, C., Sanz-Bobi, M.Á., 2011. Auto-Regressive Processes Explained by Self-Organized Maps. Application to the Detection of Abnormal Behavior in Industrial Processes. IEEE Transactions on Neural Networks. 22(12), 2078-2090.

Casali, M., Malchiodi, D., Spada, C., Zanaboni, A.M., Cotroneo, R., Furci, D., Sommariva, A., Genovese, U., Blandino, A., 2021. A Pilot Study for Investigating the Feasibility of Supervised Machine Learning Approaches for the Classification of Pedestrians Struck by Vehicles. Journal of Forensic and Legal Medicine. 84, 102256.

Chang, P.Y., Seibold, F., Thasanatorn, C., 1980. Rational Methodology for the Prediction of Structural Response Due to Collisions of Ships., United States.

Chen, Y.P., Dai, Q.J., Zhang, D.L., Bian, Z.Z., 2000. Spectral Decomposition Based on Oscillator-Array Model, 2000 5TH INTERNATIONAL CONFERENCE ON SIGNAL PROCESSING PROCEEDINGS, VOLS I-III, 5th International Conference on Signal Processing, pp. 240-243.

China, C.P.C.L., 2015. General Specifications for Design of Highway Bridges and Culverts, JTG D60-2015, Beijing.

Cho, K., van Merrienboer, B., Gulcehre, C., Bougares, F., Schwenk, H., Bengio, Y., 2014. Learning Phrase Representations Using RNN Encoder-Decoder for Statistical Machine Translation. Conference on Empirical Methods in Natural Language Processing.

Dai, L., Ehlers, S., Rausand, M., Utne, I.B., 2013. Risk of Collision Between Service Vessels and

Offshore Wind Turbines. Reliability Engineering & System Safety. 109, 18-31.
Dale, K., Bingbin, Y., 2015. Draft: FAST Ice Module Manual, University of Michigan.
De Oliveria, J., 1981. The Behavior of Steel Offshore Structures Under Accidental Collisions, Offshore Technology Conference, p. 4136.
DNVGL, 2015. Safety Principals and Arrangements, DNV-OS-A101. Det Norske Veritas, Norway.
Ellinas, C.P., 1995. Mechanics of Ship/Jack-Up Collisions. Journal of Constructional Steel Research. 33(3), 283-305.
Guo, Y., Cao, X., Liu, B., Peng, K., 2020. El Niño Index Prediction Using Deep Learning with Ensemble Empirical Mode Decomposition. Symmetry-Culture and Science. 12(6), 893.
Hinich, M.J., Foster, J., Wild, P., 2009. Discrete Fourier Transform Filters: Cycle Extraction and Gibbs Effect Considerations. Macroeconomic Dynamics. 13(4), 523-534.
Husari, F., Seshadrinath, J., 2022. Early Stator Fault Detection and Condition Identification in Induction Motor Using Novel Deep Network. IEEE Trans. Artif. Intell. 3(5), 809-818.
Jin, W.L., Song, J., Gong, S.F., Lu, Y., 2005. Evaluation of Damage to Offshore Platform Structures Due to Collision of Large Barge. Engineering Structures. 27(9), 1317-1326.
Jonkman, J., Butterfield, S., Musial, W., Scott, G., 2009. Definition of a 5-MW Reference Wind Turbine for Offshore System Development, NREL/TP-500-38060. National Renewable Energy Lab (NREL), United States.
Kammoun, M., Kammoun, A., Abid, M., 2023. LSTM-AE-WLDL: Unsupervised LSTM Auto-Encoders for Leak Detection and Location in Water Distribution Networks. Water Resour Manage. 37(2), 731-746.
Kinkead, A., 1980. A Method for Analysing Cargo Protection Afforded by Ship Structures in Collision and its Application to an Lng Carrier. Institute of Transportation Engineers.
Lee, D., Hodges, D.H., Patil, M.J., 2002. Multi-Flexible-Body Dynamic Analysis of Horizontal Axis Wind Turbines. Wind Energy. 5(4), 281-300.
Li, T., Deng, S., Zhang, K., Wei, H., Wang, R., Fan, J., Xin, J., Yao, J., 2021. A Nonintrusive Parametrized Reduced-Order Model for Periodic Flows Based on Extended Proper Orthogonal Decomposition. International Journal of Computational Methods. 18(09), 2150035.
Lindenburg, C., Winkelaar, D., 2003. Aero-Elastic Modelling of the DOWEC 6 MW Pre-Design in PHATAS.
Ma, Z., Choi, J., Sohn, H., 2023. Continuous Bridge Displacement Estimation Using Millimeter-Wave Radar, Strain Gauge and Accelerometer. Mechanical Systems and Signal Processing. 197, 110408.
Maharana, K., Mondal, S., Nemade, B., 2022. A Review: Data Pre-Processing and Data Augmentation Techniques. Global Transitions Proceedings. 3(1), 91-99.
Minorsky, V.U., 1958. An Analysis of Ship Collisions with Reference to Protection of Nuclear Power Plants. Journal of Ship Research. 3(2), 1-4.
Petersen, M.J., Pedersen, P.T., 1981. Collisions Between Ships and Offshore Platforms, Offshore Technology Conference, p. 4134.
Pule, M., Matsebe, O., Samikannu, R., 2022. Application of PCA and SVM in Fault Detection and Diagnosis of Bearings with Varying Speed. Mathematical Problems in Engineering. 2022(1), 5266054.
Radford, A., Metz, L., Chintala, S., 2015. Unsupervised Representation Learning with Deep Convolutional Generative Adversarial Networks. CoRR. abs/1511.06434
Reckling, K.A., 1983. Mechanics of Minor Ship Collisions. International Journal of Impact Engineering.

1(3), 281-299.
Rong, H., Teixeira, A.P., Guedes Soares, C., 2022. Ship Collision Avoidance Behaviour Recognition and Analysis Based On AIS Data. Ocean Engineering. 245, 110479.
Sarkar, S., Fitzgerald, B., 2020. Vibration Control of Spar-Type Floating Offshore Wind Turbine Towers Using a Tuned Mass-Damper-Inerter. Structural Control and Health Monitoring. 27(1), e2471.
Sarkar, S., Fitzgerald, B., 2021. Use of Kane's Method for Multi-Body Dynamic Modelling and Control of Spar-Type Floating Offshore Wind Turbines. Energies. 14(20), 6635.
Sei, Y., Ohsuga, A., 2021. Count Estimation with a Low-Accuracy Machine Learning Model. IEEE Internet of Things Journal. 8(8), 7079-7088.
Seizo, M., Masataka, F., Masanori, S., Matsuji, S., 1971. Equivalent Added Mass of Ships in Collisions. Selected Papers from the Journal of the Society of Naval Architects of Japan. 207(2), 309-316.
Song, M., Jiang, Z., Yuan, W., 2021. Numerical and Analytical Analysis of a Monopile-Supported Offshore Wind Turbine Under Ship Impacts. Renewable Energy. 167, 457-472.
Su, X., Cao, C., Zeng, X., Feng, Z., Shen, J., Yan, X., Wu, Z., 2021. Application of DBN and GWO-SVM in Analog Circuit Fault Diagnosis. Scientific Reports. 11(1), 7969.
Tang, Z., Chen, Z., Bao, Y., Li, H., 2019. Convolutional Neural Network-Based Data Anomaly Detection Method Using Multiple Information for Structural Health Monitoring. Structural Control & Health Monitoring. 26(1), e2296.
Tebbett, I.E., 1987. The Last Five Years' Experience in Steel Platform Repairs, Offshore Technology Conference, p. 5385.
Wei, P., Cagle, L., Reza, T., Ball, J., Gafford, J., 2018. LiDAR and Camera Detection Fusion in a Real-Time Industrial Multi-Sensor Collision Avoidance System. Electronics. 7(6), 84.
Xue, T., Zhong, M., Luo, L., Li, L., Ding, S.X., 2020. Distributionally Robust Fault Detection by Using Kernel Density Estimation. IFAC-PapersOnLine. 53(2), 652-657.
Yiakopoulos, C.T., Gryllias, K.C., Antoniadis, I.A., 2011. Rolling Element Bearing Fault Detection in Industrial Environments Based On a K-Means Clustering Approach. Expert Systems with Applications. 38(3), 2888-2911.
Zadrozny, B., Langford, J., Abe, N., 2003. Cost-Sensitive Learning by Cost-Proportionate Example Weighting. Third IEEE International Conference on Data Mining.
Zhang, L., Xiong, G., Liu, H., Zou, H., Guo, W., 2010. Bearing Fault Diagnosis Using Multi-Scale Entropy and Adaptive Neuro-Fuzzy Inference. Expert Systems with Applications. 37(8), 6077-6085.
Zhang, S., Pedersen, P.T., 1999. The Mechanics of Ship Collisions.
Zhao, Y., Ren, J., Zhang, B., Wu, J., Lyu, Y., 2023. An Explainable Attention-Based TCN Heartbeats Classification Model for Arrhythmia Detection. Biomedical Signal Processing and Control. 80(1), 104337.
Zhu, L., Faulkner, D., 1991. Numerical Modeling of Dynamic Inelastic Response of Clamped Rectangular Plates Impacted by a Knife-Edge Indentor. Journal of Offshore Mechanics and Arctic Engineering. 113(4), 312-319.
Zhu, L., Faulkner, D., Atkins, A.G., 1994. The Impact of Rectangular Plates Made from Strain-Rate Sensitive Materials. International Journal of Impact Engineering. 15(3), 245-255.
Zhu, Q., Zhang, F., Liu, S., Wu, Y., Wang, L., 2019. A Hybrid VMD–BiGRU Model for Rubber Futures Time Series Forecasting. Applied Soft Computing. 84, 105739.